Ultrasmall Blueshift of Near-Infrared Fluorescence in Phase-Stable Cs_2SnI_6 Thin Films

Ripeng Luo[1,2] Siwei Zhang,[1,2] Shichao Zhao,[3] Jingzhou Li,[1,2] Feiyu Kang,[1,2] Kuang Yu,[1,2,†] and Guodan Wei[1,2,*]

[1] *Tsinghua-Berkeley Shenzhen Institute (TBSI), Tsinghua University, Shenzhen 518055, People's Republic of China*

[2] *Tsinghua Shenzhen International Graduate School, Tsinghua University, Shenzhen 518055, People's Republic of China*

[3] *College of Materials & Environmental Engineering, Hangzhou Dianzi University, Hangzhou 310018, People's Republic of China*

Cubic Cs_2SnI_6 perovskite is considered to be an ideal lead-free and air-stable alternative to traditional $APbX_3$ [$A =$ Cs, K, CH_3NH_3, $CH(NH_2)_2$] perovskites for optoelectronic applications, such as solar cells and photodetectors. Herein, both experiments and theoretical calculations are carried out to study the lattice dynamics and temperature dependences of band gaps. Using Raman spectroscopy, we show that the obtained Cs_2SnI_6 film maintains a long-range crystalline structure of the cubic phase within 77–300 K, which is further confirmed via lattice dynamics calculations based on density functional theory (DFT). An ultrasmall net blueshift of 0.035 eV deduced from its temperature-dependent photoluminescence (PL) spectrum is observed as the temperature increases from 103 to 300 K, making it an ideal material for optoelectronic devices. Notably, this blueshift of the Cs_2SnI_6 film is significantly smaller than that of the DFT-calculated band-gap shift ($\sim$0.085 eV) based on thermal expansion theory. This deviation is attributed to the strong phonon-electron (ph-e) interaction inherently occurring in Cs_2SnI_6 material, which counterbalances the thermal expansion effects. We further evaluate the magnitude of the ph-e interaction by fitting the full width at half maximum (FWHM) of the PL spectrum. The fitted Huang-Rhys factor (S) of 4.9 is consistent with reduced electronic dimensionality and increased vibrational degree of freedom, indicating stronger ph-e coupling strength in the Cs_2SnI_6 film compared with regular $APbX_3$-type perovskites ($S < 3.3$). Adopting both thermal expansion and ph-e coupling effects, the ultrasmall band-gap shift is theoretically calculated and is in good agreement with the experimental blueshift of the band gap. In summary, our work illustrates the solid structural stability of Cs_2SnI_6 in both lattice and electronic structures, paving the way for the next generation of optoelectronic devices.

I. INTRODUCTION

Compared with conventional optoelectronic materials, the perovskite family features many great advantages, such as high band-gap tunability, solution processability, multiple micro- to nanoscales, and high carrier mobility [1]. Hence, tremendous efforts have been made to their applications in optoelectronic devices, including photodetection [2,3], light-emitting diodes [4,5], and photovoltaics [6–8]. To date, perovskite-based solar cells reach a record efficiency of 25.2%, which is comparable with state-of-the-art Si [9]. While continuing to achieve a higher conversion efficiency, the relative low stability of regular perovskite materials remains to be a long-standing concern [10,11].

Air exposure or temperature variations may lead to undesirable phase transitions that could deteriorate device performance. Therefore, a physical understanding of their phase stability is becoming more and more crucial for further development [12–14].

Cs_2SnI_6 is a derivative of $CsSnI_3$ that provides a feasible solution to phase stability. The structural stability and lattice dynamic properties of Cs_2SnI_6 have attracted broad research interests. Cs_2SnI_6 possesses high antioxidation stability due to closed-shell Sn^{4+}. As a result, half of the Sn atoms and corresponding octahedra are removed within alternate (1 1 1) planes, resulting in reduced structure dimensionality. Due to its unique structure, cubic-phase Cs_2SnI_6 has much better air stability than that of $APbX_3$ $APbX_3$ perovskite materials. Moreover, it possesses an ideal band gap with a typical value of 1.30–1.48 eV, within the near-infrared (NIR) range, making Cs_2SnI_6 a

*weiguodan@sz.tsinghua.edu.cn
†yu.kuang@sz.tsinghua.edu.cn

014048-1

promising light-absorbing [15] and infrared (IR) photodetection material [16,17]. However, the low-temperature phase-transition behavior of Cs_2SnI_6 is still under debate [18,19]. Raman spectroscopy can be an ideal approach to study such phase transitions due to its high sensitivity to long-range symmetry [20]. Temperature-dependent photoluminescence (PL) spectroscopy is of particular interest for optoelectronic materials, as it is a widespread measurement that uncovers the underlying photophysical process. Moreover, the PL spectra of materials are directly related to their potential for particular optoelectronic device applications, such as aerospace station applications. Early studies of hybrid single perovskite report an additional emission peak for $CH_3NH_3PbI_3$ at low temperature, originating from its phase transition [21]. Yu *et al.* [22] reported that band-gap variation with temperature in $CsSnI_3$ was uniquely dominated by thermal lattice expansion, while the phonon-electron (ph-*e*) coupling contribution was neglected. However, a fundamental understanding of temperature-dependent photoemissive characteristics and phonon-electron coupling strength of the vacancy-ordered double-perovskite Cs_2SnI_6 is yet to be developed.

Herein, a continuous Cs_2SnI_6 thin film deposited through a modified chemical vapor deposition (CVD) method is successfully fabricated. Raman spectroscopy combined with density functional theory (DFT) calculations confirms the long-range structural stability of the cubic phase from 77 to 300 K. Within the measured temperature range, an overall small band-gap shift is extracted from the PL spectrum. The ultrasmall blueshift of the band gap with increasing temperature for Cs_2SnI_6 is quite low compared with that of the state-of-the-art bulk materials such as PbS, making it a superior photosensitive material with a wider working temperature range [23]. Notably, DFT calculations show that the predicted blueshift value introduced by the thermal expansion effect is much larger than that of typical experimental results, unlike $CsSnI_3$ [22]. We show that this difference is attributed to strong phonon-electron coupling. The coupling strength can be partially quantified by fitting the full width at half maximum (FWHM) of the PL spectrum, through which the experimental result is reproduced with reasonable agreement. Our work demonstrates superior phase and band-gap stability of Cs_2SnI_6. With a deeper understanding of the underlying physics, we seek to provide insights and guidelines for the development of the next generation of photosensitive materials that are more robust under different working conditions.

II. EXPERIMENTAL AND COMPUTATIONAL DETAILS

All chemicals are purchased from Aladdin Corporation (Shanghai, China) and used as received. Porous anodic aluminum oxide (AAO) platelets with 0.4 μm pore size are purchased from Shangmu Tech. $10 \times 10 \times 10$ mm^3 silicon platelets with a 300-nm-thick silica layer and $15 \times 15 \times 15$ mm^3 glass platelets are employed as smooth substrates. The silicon and glass substrates are washed with detergent and later cleaned in an ultrasonic bath in deionized water, acetone, and ethanal sequentially for 15 min each. After drying under a high-pressure N_2 flow, the substrates are treated with O_2 and ultraviolet irradiation for 60 s. Cs_2SnI_6 thin films are synthesized by an aerosol-assisted chemical vapor deposition (AACVD) method, following the work of Ke *et al.* [24], with silicon, glass, and AAO substrates.

The structure and chemical composition of the Cs_2SnI_6 thin film are characterized by x-ray diffraction (XRD) and x-ray photoelectron spectroscopy (XPS). XRD analysis of the thin films is achieved with a with Bruker D8 Advance x-ray diffractometer (Cu $K\alpha$, $\lambda = 0.15\,418$ nm). The detection angle, 2θ, ranges from 10° to 60° at a step rate of 5°/min. An etching source gas cluster ion beam (GCIB) is employed for depth-resolved XPS, combining Co $K\alpha$ radiation with a scan rate of 0.02°/min. A field-effect scanning electron microscope (FESEM), HITACHI SU8010, is used to examine the surface morphology of Cs_2SnI_6 thin films with an electron acceleration voltage of 5 kV. An ultraviolet-to-visible (UV-vis) spectrophotometer (Cary 5000 UV-vis-NIR, Agilent, USA) is applied at room temperature for absorption characteristics analysis of the Cs_2SnI_6 thin films on glass. Confocal Raman microscopy (HORIBA LabRAM HR800), including Raman spectroscopy and time-integrated PL spectroscopy, is employed using 532 nm Xe lamp excitation. The power density of the incident laser is 1.5, 3.8, and 7.7 mW/μm^2. The beam size is 1.298 μm in diameter. A freezing microscopy stage (THMS600, Linkam Scientific Instruments) is used for low-temperature measurements supported by liquid nitrogen. The samples are swept from 77 to 300 K and in reverse.

Herein, the computational study is based on the Vienna *ab initio* simulation package (VASP) DFT package [25,26]. Perdew, Burke, and Ernzerhof (PBE) gradient approximation functionals [27] are employed for exchange-correlation energy calculations. Due to the nonlocality of the generalized gradient approximation (GGA) based method, we combine it with the (D3) dispersion correction to include the long-range effects of van der Waals interactions. The original structure is obtained from the Inorganic Crystal Structure Database (PDF No. 51-0466), with $a = b = c = 11.641$ Å in the cubic phase. The structure optimization calculations are carried out using a $5 \times 5 \times 5$ Monkhorst *k*-mesh matrix within the primitive Brillouin zone of the cubic phase. The plane-wave energy cutoff is set to be 700 eV. The resulting structure displays a cubic phase with a lattice constant of 11.64 Å. The first-principles lattice dynamics calculations are performed

to calculate the phonon band structure and the thermal properties of the Cs_2SnI_6 vacancy-ordered double perovskite. The harmonic force constants are calculated via $PBE + D3$ functionals implemented in the VASP package and the resulting dynamics matrix is treated by Phonopy [28]. In each displacement, the Brillouin zone is sampled with a $3 \times 3 \times 3$ mesh and the plane-wave basis energy cutoff is set to 400 eV. The temperature dependence of the free energy at 10 K intervals is calculated and treated by Phonopy. By gradually increasing the scaling factor, a series of volumes are created and atomic structures in different volumes are optimized using the same procedures mentioned above. The phonon properties and the temperature dependence of free energy at different volumes are obtained using the aforementioned method. At each temperature, the optimal volume and structure with lowest free energy are identified. The screened hybrid Heyd-Scuseria-Ernzerhof (HSE06) functional is employed in the band-gap calculations. The cutoff energy for the band-gap calculations is set to 400 eV, in conjunction with a gamma-centered $5 \times 5 \times 5$ k mesh. Unlike previous work [29,30], we adopt 25% Hartree-Fock exchange, which is the same as the original setting, without increasing it arbitrarily to fit the experiment. Electronic density of states (DOS) are plotted with a high resolution in energy (0.004 eV). In all calculations, $GGA + U$ is adopted to include the Coulombic effect of d electrons in Sn^{4+}, where U is 4 eV.

III. MATERIAL PROPERTIES AND FILM MORPHOLOGIES

As shown in Fig. 1(a), the B sites are constituted by Sn atoms and vacancies, forming alternating crystal planes, parallel to the (1 1 1) family of lattice planes. The Sn-occupied (1 1 1) planes [blue planes in Fig. 1(a)] are separated by vacancy-occupied (1 1 1) planes, giving rise to certain unique characteristics of the Cs_2SnI_6 double perovskite. The nearest Sn-Sn distance within the (1 1 1) planes is 8.22 Å, while the lattice constant is 11.64 Å at room temperature. The structure of Cs_2SnI_6 demonstrates a significantly increased Sn-Sn distance and largely reduced dimensionality relative to its single perovskite parent, $CsSnI_3$. The XRD peaks are in good agreement with calculated Cs_2SnI_6 cubic crystal facets. Figure 1(b) indicates that the thin-film samples are composed of impurity-free Cs_2SnI_6. Importantly, the relative intensity of each XRD peaks is recognized, and the peak intensity of the (1 1 1) crystal facet family is significantly enhanced compared with other facets, indicating oriented crystallization along the ⟨1 1 1⟩ direction. As shown in Fig. 1(b), no peak position changes or newly emerging peaks are observed after exposure for 2–6 weeks to an ambient environment, except for a decrease in peak intensity. This observation suggests that pure cubic Cs_2SnI_6 remains stable in air

without further protection or encapsulation steps. Depth-resolved XPS, as shown in Figs. 1(c) and 1(d), reveals slight chemical composition changes after 6 weeks. The XPS results support the air stability observed by XRD, indicating structural stability features.

According to Kaltzoglou *et al.* [15], only the three main first-order normal Raman modes of the cubic phase are displayed in the Raman spectrum of Cs_2SnI_6, as shown in Fig. 1(e). All of these Raman bands are associated with vibrations within the octahedra [31], namely, $\nu(A_{1g})$, $\nu(E_g)$, and $\delta(F_{2g})$. The phonon mode $\nu(A_{1g})$ represents the Sn—I symmetry stretching at 126 cm^{-1}, $\nu(E_g)$ represents the Sn—I asymmetry stretching at 92 cm^{-1}, and $\delta(F_{2g})$ represents the asymmetric bending I-Sn-I deformation at 78 cm^{-1}. The Raman band show good accordance with a cubic-phase Cs_2SnI_6 structure in an ambient environment. These values for Raman-active modes are in good agreement with values of 116, 90, and 77 cm^{-1} extracted from the phonon density of state, calculated by DFT lattice dynamics via the PBEsol exchange-correlation functional [28] [Fig 1(e)]. Obtaining the degree of linearity between the direct Tauc $[F(R\hbar v)]^2$ and $\hbar v(\hbar$ is the reduced Planck constant), we obtain a band gap from the intersection point with a value of 1.328 eV [Fig. 1(f)], confirming a direct electronic transition nature. The PL spectrum is recorded under 532 nm excitation with a Lorentz-Gaussian distribution shape centered at 1.40 eV.

The Cs_2SnI_6 thin films are prepared by an aerosol-assisted CVD method with both silicon and nanoporous AAO substrates. Figures 2(a) and 2(b) are SEM images of Cs_2SnI_6 on silicon substrates. The enlarged SEM image in Fig. 2(b) suggests that the thin film in Fig. 2(a) is composed of stacks of small octahedral crystal particles. Derived from previous discussions, Sn-occupied (1 1 1) planes in the Cs_2SnI_6 lattice have the highest Sn density with the shortest Sn-Sn distance. XRD results suggest that Cs_2SnI_6 tends to grow along its ⟨1 1 1⟩ direction, indicating that oriented growth of octahedral Cs_2SnI_6 single-crystalline particles is due to its intrinsic crystal configuration with Sn-occupied (1 1 1) planes. To allow for continuous growth of Cs_2SnI_6 films, nanoporous AAO platelets are applied as substrates under the same growth conditions. As shown in Figs. 2(c) and 2(d), templated by the AAO substrate, the as-obtained Cs_2SnI_6 film has a continuous network along the AAO edge, indicating that the crystal nucleus accumulates and grows inwards in the pores until they are fully covered.

IV. PHASE STABILITY AND LATTICE DYNAMICS CALCULATIONS

Figure 3(a) presents the Raman spectra of Cs_2SnI_6 from 77 to 300 K. The temperature-dependent band positions and intensity are plotted in Fig. 3(b), as the temperature increases from 77 to 300 K. The band positions with vibration modes of $\nu(A_{1g})$, $\nu(E_g)$, and $\delta(F_{2g})$ shift negatively
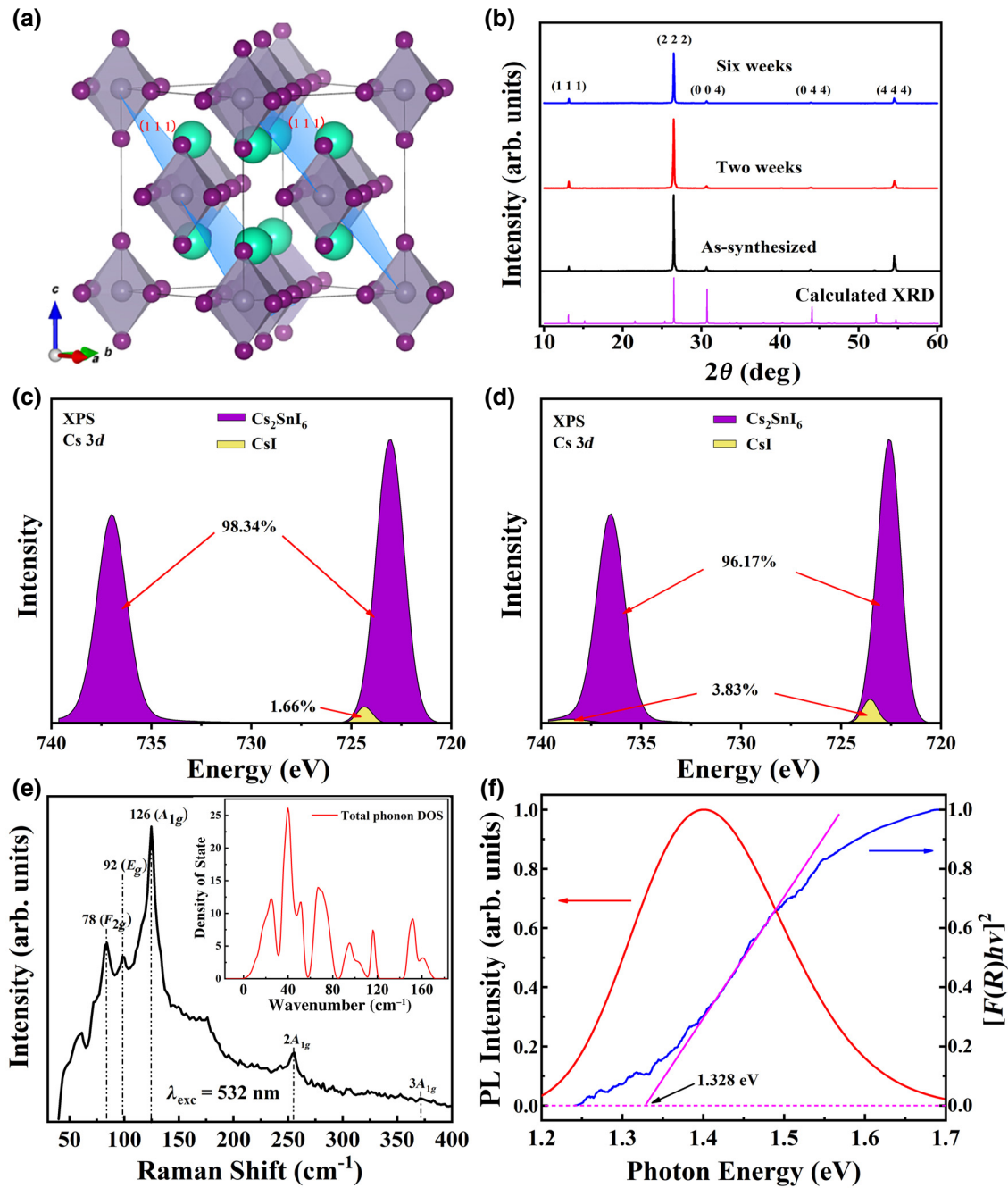
FIG. 1. (a) Schematic representation of Cs_2SnI_6 vacancy-ordered metal-halide double perovskite in cubic phase. Green, purple, and gray atoms represent Cs, I, and Sn elements, respectively. Blue parallel planes are the (1 1 1) lattice planes, aligning discrete Sn-centered octahedra. (b) XRD spectrum of the as-synthesized, two-week-deposited, and six-week-deposited Cs_2SnI_6 samples. XPS patterns of fresh (c) and two-week-deposited (d) Cs_2SnI_6 thin film in ambient environment. (e) Nonresonant Raman scattering spectrum with Raman-active modes [$\delta(F_{2g})$, $\nu(E_g)$, $\nu(A_{1g})$] and second and third modes of A_{1g}. Inset presents the total phonon DOS computed using DFT. (f) PL and absorption spectra of Cs_2SnI_6 thin film recorded at 300 K.

with temperature, as it is commonly expected that chemical bonds defreeze and soften as temperature increases. The first-order and second-order symmetric stretching modes of the Sn—I bond [$\nu(A_{1g})$] at 126.5 and 253 cm^{-1} remain consistent at all temperatures, providing direct evidence for the long-range cubic symmetry of Cs_2SnI_6. Notably, the coupled weak side bands at 113 and 153 cm^{-1} are impurity signals from CsI [32] and SnI$_4$ [33,34], respectively, corresponding to their symmetric stretching modes (ν_1). Due to the high absorption coefficient of the material,
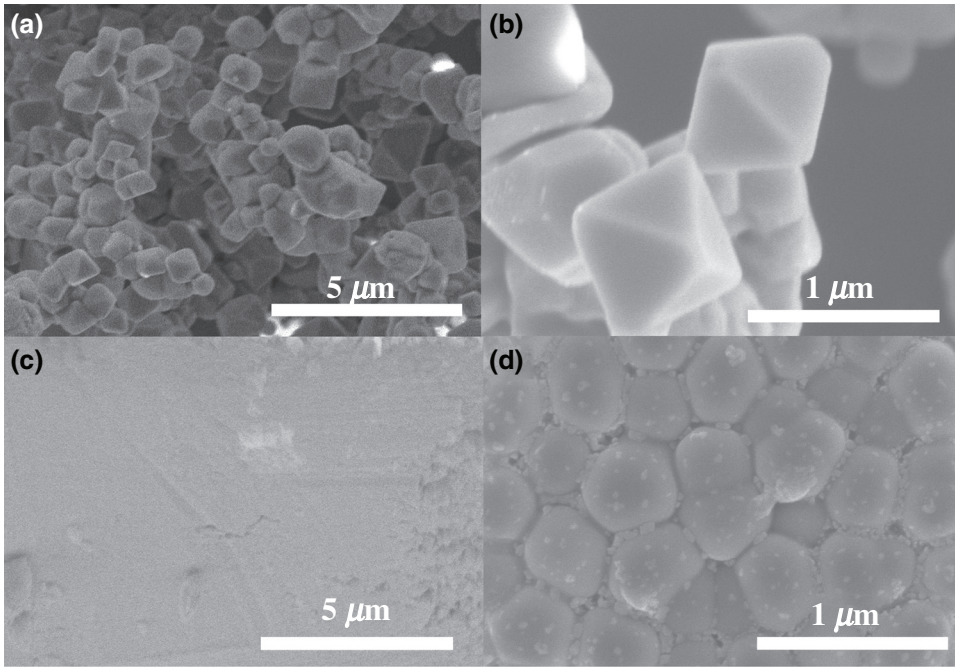
FIG. 2. (a),(b) SEM images of Cs_2SnI_6 thin film grown on silicon-silica substrate. (c),(d) SEM images of Cs_2SnI_6 thin film grown on nanoporous AAO substrate.

it decomposes into CsI and SnI_4 at all temperatures, if extensively exposed to the laser. Low-temperature Raman from other spots is presented in Figs. S1(a) and (b) within the Supplemental Material [47]. Except for impurities at 113 cm^{-1} and 153 cm^{-1}, all bands at other spots are consistent with Figs. 3(a). In Fig. 3(c), we show the phonon band structure computed using DFT. We find no imaginary frequencies at any reciprocal points, indicating that cubic-phase Cs_2SnI_6 is mechanically stable at 0 K.

To understand the physical origin of the ultrastable properties of Cs_2SnI_6, we further calculate the phonon bands in different volumes and obtain the thermal expansion coefficient using the quasiharmonic approximation (QHA) [28]. In the QHA, the Helmholtz free energy is computed as

$$H(V) = U_e(V) + F_{\text{phonon}}(V, T). \qquad (1)$$

Here, U_e is the static electronic energy and F_{phonon} is the phonon free energy, which is evaluated using the harmonic approximation. In Fig. 3(d), the volume dependence of the free energy is pictured by the relative lattice constant, where 1.000 represents the lattice constant at 10 K ($a_0 = 11.60$ Å). The equilibrium volumes are then determined by minimizing $H(V)$ at given temperatures. The black curve connects the free energy minimum at a given temperature, resulting in a thermal expansion ratio of 4×10^{-5} K^{-1}. This value is larger than the value of 2.78×10^{-5} K^{-1} for $Cs_2BiAgBr_6$.[35], which is consistent with the soft nature of Cs_2SnI_6, as previously reported [29].

V. TEMPERATURE DEPENDENCE OF THE BAND GAP

The PL emission spectra of Cs_2SnI_6 are then measured from 103 to 300 K [see Fig. 4(a)] and a net blueshift of around 0.035 eV, with a shift ratio of 0.18 meV/K, is observed. Moreover, the ultrasmall band-gap shift is consistently observed at different spots on the sample surface. As shown in Figs. S1(c)–S1(e) [47], comparable shift coefficients from other spots are consistent with our reported result (0.035 eV from 100 to 300 K). This value is much smaller than that of its parental single perovskite ($CsSnI_3 \sim 0.3$ meV/K) [22] or other state-of-the-art IR materials [23,31], which have typical shift ratios of 0.2–0.5 meV/K. Optoelectronic devices are composed of multiple active layers with stacked band gaps to form junctions for photon absorption, carrier separation, and charge transport. Therefore, the band-gap stability of active semiconductor materials with varied operation temperatures are of great importance for accuracy and endurance control, in terms of wide-temperature-range photosensitive devices, such as sensors, solar cells, and photodetectors.

Once the temperature-dependent volumes are obtained [Fig. 3(d)], single-point calculations, using a hybrid functional, are conducted to predict the band-gap shifts due to thermal expansion. The HSE06 functional (25% exact exchange) is employed as the major method in DFT calculations. The predicted average band gap with the hybrid functional HSE06 is about 0.92 eV, which is lower than the experimental value of 1.3–1.48 eV, due to the self-interaction error [36]. The resulting band structure and DOS are plotted in Fig. 4(b) and atom-site projected DOS are plotted in Fig. 4(c). According to the projected DOS,
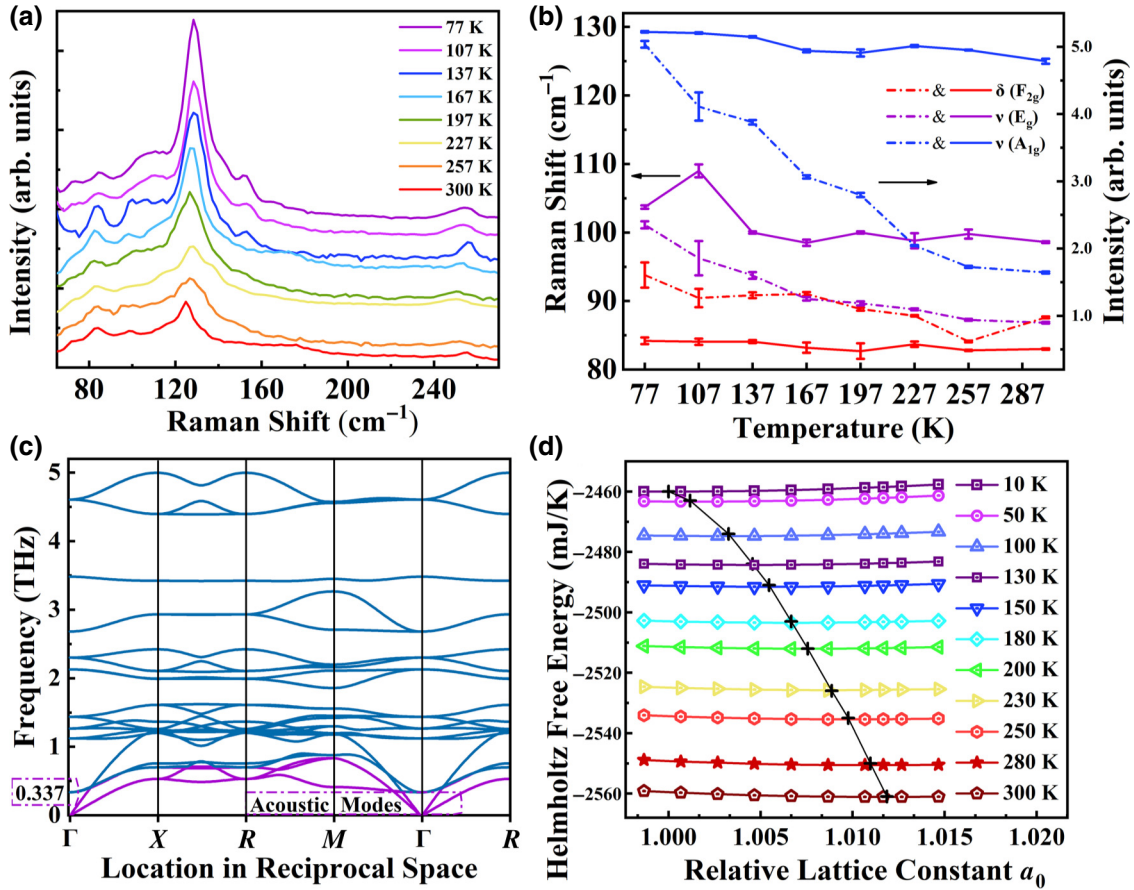
FIG. 3.   Temperature dependence of crystal structure and phase stability of Cs_2SnI_6. (a) Temperature-dependent steady-state Raman scattering spectrum recorded from 77 to 300 K at 532 nm excitation. (b) Wave numbers and intensity of the three main Raman-active vibration modes $[\nu(A_{1g}), \nu(E_g), \delta(F_{2g})]$ plotted against temperature, extracted from the steady-state Raman spectrum. Error bars represent fitting standard errors. (c) DFT-computed phonon band structure of cubic-phase Cs_2SnI_6. (d) Computed free energy profiles at different temperatures; black curve illustrates the volume thermal expansion.

the valence band edge (VBE) of Cs_2SnI_6 is mainly composed of I $5p$ bands, slightly mixing with the Sn $5p$ and Sn $4d$ bands. The conduction band edge (CBE) mainly features the Sn $5s$ orbitals, mixing with the I $5p$ bands from the Sn-I σ^* antibonding orbitals. Correspondingly, the dispersion of valence-band states is dominantly originating from the close-packed I framework. Overlap of the dispersive conduction-band states in Cs_2SnI_6 is dictated by adjacent Sn octahedra.

When the temperature increases, a net blueshift occurs [Fig. 4(b)], in agreement with the trend of the PL spectrum qualitatively. Since the thermal expansion of the volume is almost linear, the resulting blueshift also behaves linearly with respect to temperature, similar to $CsSnI_3$ reported by Yu *et al.* [22]. Quantitatively, the predicted band gap by HSE06 will increase 0.085 eV with a temperature coefficient of 425 μeV K^{-1}, which results from a typical thermal expansion effect. This shift of the band gap is consistently validated with three different functions (i.e., HSE06, HSE12, or PBE), as shown in Fig. 4(d). To study the effect

of the self-interaction error on the magnitude of the band-gap shift, the exact exchange ratio is increased to 35% with a band-gap value of 1.34 eV. The predicted band gap shifts by 0.088 eV, which is comparable to that calculated by 25%, indicating that the self-interaction effect in DFT plays a minor part in predicting the shift value. All calculated band-gap shift is consistent and significantly larger than that of the experimental value, which is only 0.035 eV [Fig. 5(d)]. An overestimation of about 0.05 eV for the band-gap shift suggests an additional factor besides thermal expansion is playing a critical role in the temperature dependence of the Cs_2SnI_6 electronic structure. According to Cordana, the band-gap shift with respect to temperature is composed of two parts of thermal expansion and phonon-electron coupling [37]:

$$\frac{\partial E_g}{\partial T} = \frac{\partial E_g}{\partial V}\frac{\partial V}{\partial T} + \sum_{j,\vec{q}}^{n}\left(\frac{\partial E_g}{\partial n_{j,\vec{q}}}\right)\left(n_{j,\vec{q}} + \frac{1}{2}\right), \quad (2)$$
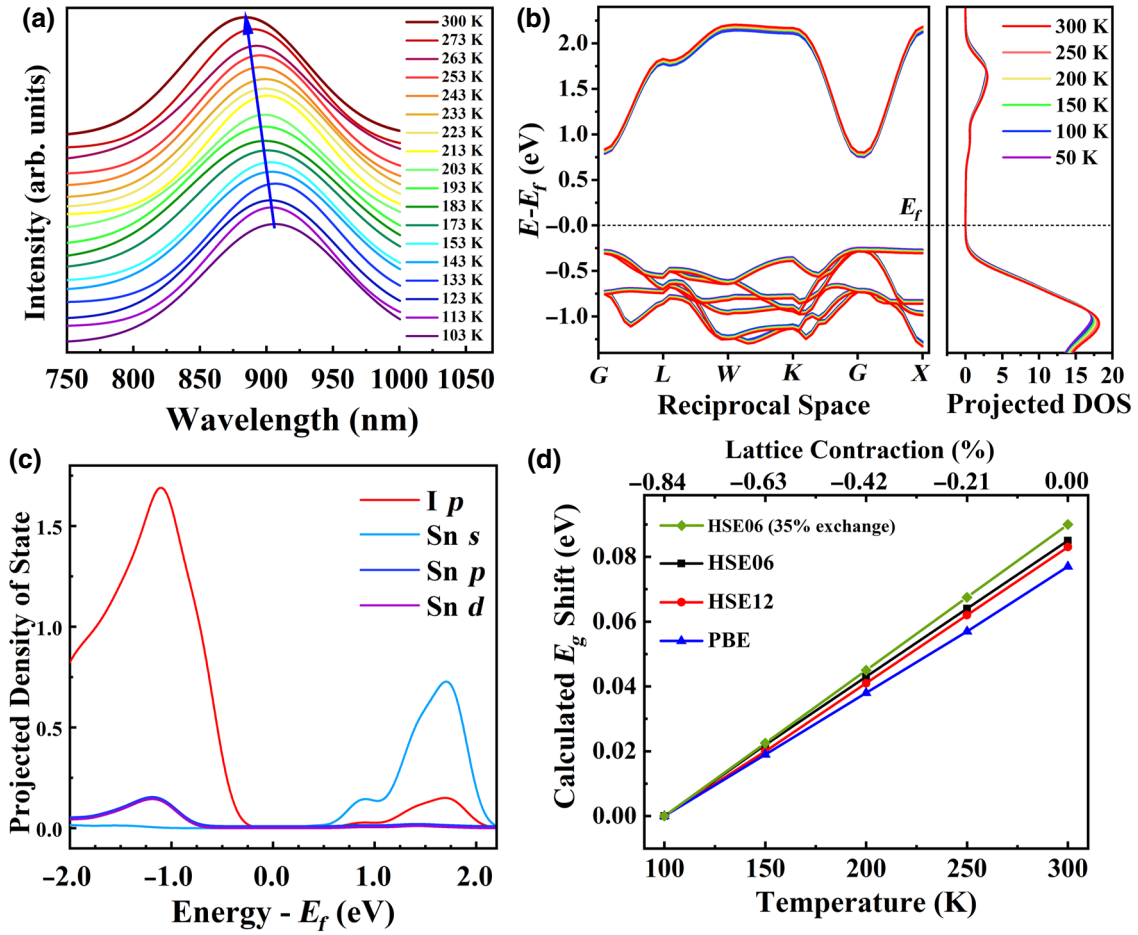
FIG. 4. Temperature dependence of the electronic structure and fluorescence of Cs_2SnI_6. (a) Fitted time-integrated photoluminescence of Cs_2SnI_6 recorded from 103 to 300 K at 532 nm excitation. (b) Calculated electronic band structure and DOS at different temperatures. (c) Partial DOS of Cs_2SnI_6 projected to different elements and different angular momentum channels. (d) Band-gap shift predictions with different density functionals.

where $n_{j,\vec{q}}$ is the phonon number in the jth branch with wave vector $\vec{q}$. Here, the first term describes the thermal expansion, while the second term accounts for the ph-e coupling. Apparently, different from its single-perovskite counterpart, $CsSnI_3$, ph-e coupling is a nontrivial factor in Cs_2SnI_6. Notably, the second ph-e coupling term in Eq (2) is computationally very expensive to quantify in an *ab initio* way; thus we adopt an empirical model, which is detailed in Sec. VI.

VI. DISCUSSION

Assuming linear thermal expansion and a single characteristic frequency for all phonons, the O'Donnell and Chen description of ph-e coupling [38] is adopted to evaluate the temperature dependence of the band gap:

$$E_g(T) = E_g(0) + \varepsilon_v \, \Delta T - \frac{2S \langle \hbar w \rangle}{e^{\frac{\langle \hbar w \rangle}{k_B T}} - 1}, \qquad (3)$$

where $E_g(0)$ is the static band gap at 0 K, ε_V is the linear coefficient due to lattice expansion, and $\langle \hbar \omega \rangle$ is the fitted average phonon energy. The theoretical ε_V obtained from the first-principles calculation is $425 \, \mu eV \, K^{-1}$. Dimensionless S is the Huang-Rhys factor [39], which measures the ph-e coupling strength due to nuclei coordinate displacement. The potential-energy surface of the electronic state is a function of the vibrational coordinate. The Huang-Rhys factor represents the ratio of the transitional energy by vibrational coordinate displacement to the phonon energy, $\hbar \omega$, within light absorption and photoluminescence.

To quantify the band-gap shift in Cs_2SnI_6, we investigate the PL peak width to obtain the Huang-Rhys factor. As shown in Fig. 5(a), the PL line width increases monotonically from 0.168 eV at 103 K to 0.220 eV at 300 K. At higher temperature, the strong ph-e coupling effect is enhanced with increasing phonon population, broadening the electronic spectrum. Herein, we relate the temperature dependence of the FWHM with the Einstein frequency as
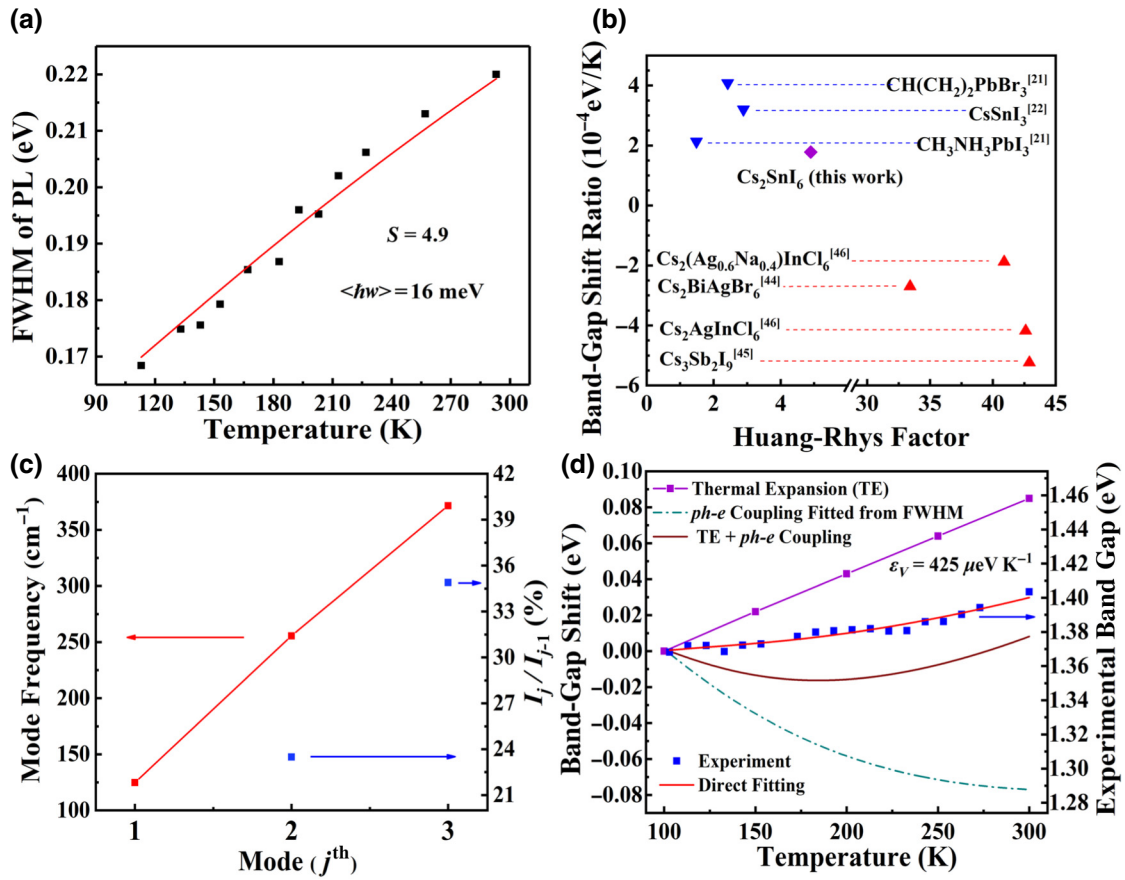
FIG. 5. (a) Temperature dependence of Cs_2SnI_6 emission line width. Data of PL FWHM are treated as functions of temperature, using Eq. (3) to fit data. Huang-Rhys factor is 4.9 and the phonon energy is 16 meV. (b) Huang-Rhys factor fitted by PL FWHM versus band-gap shift ratio for different perovskites [21,22,44–46]. (c) Frequency and relative intensity of harmonic Raman modes. (d) Temperature dependence of experimental and theoretical band gaps. Redshift by ph-*e* coupling is combined with calculated band-gap shift for comparison with experimental results.

follows [40]:

$$\Gamma(T) = 2.36 \langle \hbar w \rangle \left[S \coth \left(\frac{\langle \hbar w \rangle}{2kT} \right) \right]^{\frac{1}{2}}, \qquad (4)$$

where $\langle \hbar \omega \rangle$ is the average optical phonon energy (16 meV) and S is the Huang-Rhys factor (4.9) fitted from Eq (4). In Fig. 5(b), the Huang-Rhys factors of a variety of typical "single" and "double" perovskites are listed for comparison. The Huang-Rhys factors for single perovskites (both hybrid and inorganic) fall into the range of 1.5–3.3, while the values are over 30 for typical double perovskites (e.g., $Cs_2BiAgBr_6$ and $Cs_2AgInCl_6$). This comparison reveals that Cs_2SnI_6 delivers a median value among the halide perovskite family. Accordingly, its ph-*e* coupling strength is found to be much weaker than that of the double perovskites, but stronger than most of the single perovskites. Structurally, Cs_2SnI_6 is an intermediate species between the two limits, with ordered vacancies occupying half of

the Sn sites. Owing to the absence of prolonged polyhedral connectivity of octahedra, the vacancy-ordered double perovskite has a smaller overlap of dispersive conduction-band states, reduced electronic dimensionality, and higher atomic vibration degrees of freedom [41]. As a result, these interaction factors are likely to lead to an increased Huang-Rhys factor and stronger ph-*e* coupling strength of Cs_2SnI_6 compared with that of regular perovskites, such as $CH(CH_2)_2PbBr_3$, $CsSnI_3$, and $CH_3NH_3PbI_3$ [Fig. 5(b)].

On the other hand, a double perovskite, such as $Cs_2BiAgBr_6$, possesses a complex lattice vibrational mode within binary isolated octahedra and an indirect electronic band structure, which could give rise to enhanced ph-*e* coupling. Moreover, in the nonresonant Raman spectrum, multiphonon processes can be used as another indicator to evaluate the ph-*e* coupling strength. The Fröhlich interaction can be evaluated through the relative intensity between the two-phonon and one-phonon peaks [i.e., $I(1A_{1g})/I(2A_{1g})$] [42,43]. As shown in Fig. 5(c), the relative intensity is 24% for Cs_2SnI_6, which is smaller than

that of $Cs_2BiAgBr_6$ (over 30%) [44]. This shows a weaker ph-e coupling in Cs_2SnI_6 compared with that of double perovskites, which is consistent with our previous analysis of Fig. 5(b), wherein the Huang-Rhys factor of Cs_2SnI_6 falls into the intermediate region between those of regular ABX_3 and double perovskites.

After verifying our FWHM fitting process, the fitted Huang-Rhys factor (S) and the Einstein phonon energy ($\hbar\omega$) are then inserted into Eq (3), resulting in a 0.077 eV redshift as the temperature increases from 103 to 300 K. In Fig. 5(d), we combine the band-gap shifts introduced by thermal expansion and ph-e coupling fitted from the FWHM and compare them with the experimental results. The qualitative trend is well reproduced, although we slightly underestimate the band-gap shift by about 0.02 eV. We note that the ultrasmall band-gap shifts rely on the delicate cancellation of two effects, and hence, their exact evaluation require a highly accuracy estimation of ph-e coupling. Extremely expensive calculations are needed to compute all coupling matrix elements, which are beyond the scope of the largely simplified Einstein model used in this work. Nevertheless, a reasonable semiquantitative agreement is achieved, showing that ph-e coupling is indeed playing a crucial role in cancelling out the thermal expansion effects to pin the band gap. Notably, an ultrasmall band-gap shift is measured from the temperature-dependent PL spectrum which is recorded in a well-controlled inert environment at low pressure and humidity, and therefore, the thermal stability of a practical optical device applying Cs_2SnI_6 needs to be further addressed under ambient conditions.

VII. CONCLUSIONS

A high-quality Cs_2SnI_6 thin film is successfully deposited using a modified CVD method. Both temperature-dependent Raman and lattice dynamics calculations confirm a stable cubic phase with long-range symmetry from 77 to 300 K. The temperature-dependent PL spectrum characterizes a blueshift of the band gap as small as 0.035 eV from 103–300 K, showing feasible photoluminescence stability over a wide range of temperatures. Quantitatively, DFT calculations predict that the band gap of Cs_2SnI_6 will increase to 0.085 eV as the temperature increases to 300 K, if only taking into account the thermal expansion effect, which is significantly larger than the experimental value of 0.035 eV. An overestimation of about 0.05 eV for the band-gap shift suggests an additional factor besides thermal expansion is playing a critical role in the temperature dependence of the Cs_2SnI_6 electronic structure, which is closely related to its internal structure, with ordered vacancies occupying half of the Sn sites. Correspondingly, it has a smaller overlap of dispersive conduction band states, reduced electronic dimensionality, and higher atomic vibration degrees of

freedom, leading to an increased phonon-electron interaction. As a result, the fitted Huang-Rhys factor ($S = 4.9$) from the temperature-dependent PL width of Cs_2SnI_6 films is obtained and indicates stronger phonon-electron coupling strength compared with that of regular $APbX_3$-type perovskites ($S < 3.3$). In combining thermal expansion (blueshift) and phonon-electron effects (redshift), we calculate a stable band-gap shift that is in reasonable agreement with experimental data. Therefore, the small overall temperature coefficient of Cs_2SnI_6 is pinned through mutual cancellation of thermal expansion and phonon-electron coupling. This physical origin of the structural and optical stability for the as-prepared Cs_2SnI_6 film sheds light on the next generation of practical optoelectronic applications.

[1] X. He, Y. Qiu, and S. Yang, Fully-inorganic trihalide perovskite nanocrystals: A new research frontier of optoelectronic materials, Adv Mater. **29,** 1700775 (2017).

[2] L. Dou, Y. M. Yang, J. You, Z. Hong, W. H. Chang, G. Li, and Y. Yang, Solution-processed hybrid perovskite photodetectors with high detectivity, Nat Commun. **5,** 5404 (2014).

[3] H. L. Zhu, Z. Liang, Z. Huo, W. K. Ng, J. Mao, K. S. Wong, W.-J. Yin, and W. C. H. Choy, Low-bandgap methylammonium-rubidium cation Sn-rich perovskites for efficient ultraviolet-visible-near infrared photodetectors, Adv. Funct. Mater. **28,** 1706068 (2018).

[4] S. A. Veldhuis, P. P. Boix, N. Yantara, M. Li, T. C. Sum, N. Mathews, and S. G. Mhaisalkar, Perovskite materials for light-emitting diodes and lasers, Adv Mater. **28,** 6804 (2016).

[5] R. Ben Aich, I. Saïdi, S. Ben Radhia, K. Boujdaria, T. Barisien, L. Legrand, F. Bernardot, M. Chamarro, and C. Testelin, Bright-exciton Splittings in Inorganic Cesium Lead Halide Perovskite Nanocrystals, Phys. Rev. Appl. **11,** 034042 (2019).

[6] N. J. Jeon, H. Na, E. H. Jung, T.-Y. Yang, Y. G. Lee, G. Kim, H.-W. Shin, S. Il Seok, J. Lee, and J. Seo, A fluorene-terminated hole-transporting material for highly efficient and stable perovskite solar cells, Nat. Energy **3,** 682 (2018).

[7] Z. Xiao, W. Meng, J. Wang, D. B. Mitzi, and Y. Yan, Searching for promising new perovskite-based photovoltaic absorbers: The importance of electronic dimensionality, Mater. Horiz. **4,** 206 (2017).

[8] X.-G. Zhao, D. Yang, J.-C. Ren, Y. Sun, Z. Xiao, and L. Zhang, Rational design of halide double perovskites for optoelectronic applications, Joule **2,** 1662 (2018).

[9] Best Research-Cell Efficiency Chart, (The National Renewable Energy Laboratory) https://www.nrel.gov/pv/cell-efficiency.html (Accessed 2019.11.06).

[10] J. Kangsabanik, S. Ghorui, M. Aslam, and A. Alam, Optoelectronic Properties and Defect Physics of Lead-Free Photovoltaic Absorbers $Cs_2Au^IAu^{III}X_6$ (X = I, Br), Phys. Rev. Appl. **13**, 014005 (2020).

[11] T. Li, X. Zhao, D. Yang, M.-H. Du, and L. Zhang, Intrinsic Defect Properties in Halide Double Perovskites for Optoelectronic Applications, Phys. Rev. Appl. **10**, 041001 (2018).

[12] Y. Cai, W. Xie, H. Ding, Y. Chen, K. Thirumal, L. H. Wong, N. Mathews, S. G. Mhaisalkar, M. Sherburne, and M. Asta, Computational study of halide perovskite-derived A_2BX_6 inorganic compounds: Chemical trends in electronic structure and structural stability, Chem. Mater. **29**, 7740 (2017).

[13] E. L. da Silva, J. M. Skelton, S. C. Parker, and A. Walsh, Phase stability and transformations in the halide perovskite $CsSnI_3$, Phys. Rev. B **91**, 144107 (2015).

[14] N. Gross, Y.-Y. Sun, S. Perera, H. Hui, X. Wei, S. Zhang, H. Zeng, and B. A. Weinstein, Stability and Band-gap Tuning of the Chalcogenide Perovskite $BaZrS_3$ in Raman and Optical Investigations at High Pressures, Phys. Rev. Appl. **8**, 044014 (2017).

[15] A. Kaltzoglou, M. Antoniadou, A. G. Kontos, C. C. Stoumpos, D. Perganti, E. Siranidi, V. Raptis, K. Trohidou, V. Psycharis, M. G. Kanatzidis, and P. Falaras, Optical-vibrational properties of the Cs_2SnX_6 (X = Cl, Br, I) defect perovskites and hole-transport efficiency in dye-sensitized solar cells, J. Phys. Chem. C **120**, 11777 (2016).

[16] S. Ghosh, S. Paul, and S. K. De, Control synthesis of air-stable morphology tunable Pb-free Cs_2SnI_6 perovskite nanoparticles and their photodetection properties, Part Part Syst. Char. **35**, 1800199 (2018).

[17] A. F. Wang, X. X. Yan, M. Zhang, S. B. Sun, M. Yang, W. Shen, X. Q. Pan, P. Wang, and Z. T. Deng, Controlled synthesis of lead-free and stable perovskite derivative Cs_2SnI_6 nanocrystals via a facile hot-injection process, Chem. Mater. **28**, 8132 (2016).

[18] A. E. Maughan, A. M. Ganose, M. A. Almaker, D. O. Scanlon, and J. R. Neilson, Tolerance factor and cooperative tilting effects in vacancy-ordered double perovskite halides, Chem. Mater. **30**, 3909 (2018).

[19] U.-G. Jong, C.-J. Yu, Y.-H. Kye, S.-H. Choe, J.-S. Kim, and Y.-G. Choe, Anharmonic phonons and phase transitions in the vacancy-ordered double perovskite Cs_2SnI_6 from first-principles predictions, Phys. Rev. B **99**, 184105 (2019).

[20] I. W. D. F. SHRIVER, Vibrational frequencies and intramolecular forces in anionic tin-halogen complexes and related species, Inorg. Chem. **8**, 914 (1969).

[21] M. I. Dar, G. Jacopin, S. Meloni, A. Mattoni, N. Arora, A. Boziki, S. M. Zakeeruddin, U. Rothlisberger, and M. Gratzel, Origin of unusual bandgap shift and dual emission in organic-inorganic lead halide perovskites, Sci Adv. **2**, 1601156 (2016).

[22] C. Yu, Z. Chen, J. J. Wang, W. Pfenninger, N. Vockic, J. T. Kenney, and K. Shum, Temperature dependence of the band gap of perovskite semiconductor compound $CsSnI_3$, J. Appl. Phys. **110**, 063526 (2011).

[23] H. J. Lian, A. Yang, M. L. W. Thewalt, R. Lauck, and M. Cardona, Effects of sulfur isotopic composition on the band gap of PbS, Phys. Rev. B **73**, 233202 (2006).

[24] J. C. R. Ke, D. J. Lewis, A. S. Walton, B. F. Spencer, P. O'Brien, A. G. Thomas, and W. R. Flavell, Ambient-air-stable inorganic Cs_2SnI_6 double perovskite thin films via aerosol-assisted chemical vapour deposition, J. Mater. Chem. A **6**, 11205 (2018).

[25] G. Kresse and J. Hafner, Ab initio molecular dynamics for liquid metals, Phys. Rev. B **47**, 558 (1993).

[26] G. Kresse and J. Hafner, Ab initio molecular-dynamics simulation of the liquid-metal–amorphous-semiconductor transition in germanium, Phys. Rev. B **49**, 14251 (1994).

[27] J. P. Perdew, K. Burke, and M. Ernzerhof, Generalized Gradient Approximation Made Simple, Phys. Rev. Lett. **77**, 3865 (1996).

[28] A. Togo and I. Tanaka, First principles phonon calculations in materials science, Scr. Mater. **108**, 1 (2015).

[29] M. Rasukkannu, D. Velauthapillai, and P. Vajeeston, A first-principle study of the electronic, mechanical and optical properties of inorganic perovskite Cs_2SnI_6 for intermediate-band solar cells, Mater. Lett. **218**, 233 (2018).

[30] B. Saparov, J. P. Sun, W. W. Meng, Z. W. Xiao, H. S. Duan, O. Gunawan, D. Shin, I. G. Hill, Y. F. Yan, and D. B. Mitzi, Thin-film deposition and characterization of a Sn-deficient perovskite derivative Cs_2SnI_6, Chem. Mater. **28**, 2315 (2016).

[31] M. J. Ashley, M. N. O'Brien, K. R. Hedderick, J. A. Mason, M. B. Ross, and C. A. Mirkin, Templated synthesis of uniform perovskite nanowire arrays, J. Am. Chem. Soc. **138**, 10096 (2016).

[32] M. R. Mohammad and W. F. Sherman, Raman and resonance-Raman spectra of CsI/I_3^-, J. Mol. Struct. **115**, 27 (1984).

[33] H. Stammreich, R. Forneris, and Y. Tavares, Raman spectra and force constants of GeI_4 and SnI_4, 25, 1278, (1956).

[34] M. L. Delwaulle, M. B. Buisset, and M. Delhaye, The study of chloroiodides of silicon, tin and germanium using the Raman spectra as proof of equilibria, J. Am. Chem. Soc. **74**, 5768 (1952).

[35] L. Dong, S. Sun, Z. Deng, W. Li, F. Wei, Y. Qi, Y. Li, X. Li, P. Lu, and U. Ramamurty, Elastic properties and thermal expansion of lead-free halide double perovskite $Cs_2AgBiBr_6$, Comput. Mater. Sci. **141**, 49 (2018).

[36] E. Ruiz, S. Alvarez, J. Cano, and V. Polo, About the calculation of exchange coupling constants using density-functional theory: The role of the self-interaction error, J. Chem. Phys. **123**, 164110 (2005).

[37] M. Cardona, Electron–phonon interaction in tetrahedral semiconductors, Solid State Commun. **133**, 3 (2005).

[38] K. P. O'Donnell and X. Chen, Temperature dependence of semiconductor band gaps, Appl. Phys. Lett. **58**, 2924 (1991).

[39] K. Huang, A. Rhys, and N. F. Mott, Theory of light absorption and non-radiative transitions in F-centres, Proc. R. Soc. Lond. 204, 406 (1950).

[40] W. B. Fowler, Physics of Color Centers (1968).

[41] A. E. Maughan, A. M. Ganose, D. O. Scanlon, and J. R. Neilson, Perspectives and design principles of vacancy-ordered double perovskite halide semiconductors, Chem. Mater. **31**, 1184 (2019).

[42] C. M. Iaru, J. J. Geuchies, P. M. Koenraad, D. Vanmaekelbergh, and A. Y. Silov, Strong carrier-phonon coupling in lead halide perovskite nanocrystals, ACS Nano **11**, 11024 (2017).

[43] Q. Zhang, J. Zhang, M. I. B. Utama, B. Peng, M. de la Mata, J. Arbiol, and Q. Xiong, Exciton-phonon coupling in individual ZnTe nanorods studied by resonant Raman spectroscopy, Phys. Rev. B **85**, 085418 (2012).

[44] J. A. Steele, P. Puech, M. Keshavarz, R. Yang, S. Banerjee, E. Debroye, C. W. Kim, H. Yuan, N. H. Heo, J. Vanacken, A. Walsh, J. Hofkens, and M. B. J. Roeffaers, Giant electron–phonon coupling and deep conduction band resonance in metal halide double perovskite, ACS Nano **12**, 8081 (2018).

[45] K. M. McCall, C. C. Stoumpos, S. S. Kostina, M. G. Kanatzidis, and B. W. Wessels, Strong electron–phonon coupling and self-trapped excitons in the defect halide perovskites $A_3M_2I_9$ (A = Cs, Rb; M = Bi, Sb), Chem. Mater. **29**, 4129 (2017).

[46] J. Luo *et al.*, Efficient and stable emission of warm-white light from lead-free halide double perovskites, Nature **563**, 541 (2018).

[47] See the Supplemental Material at http://link.aps.org/supplemental/10.1103/PhysRevApplied.14.014048 for Supplemental Raman and PL spectrum on the sample surface.